Journal of Applied Physics

Plasma potential of a moving ionization zone in DC magnetron sputtering

Cite as: J. Appl. Phys. **121**, 063302 (2017); https://doi.org/10.1063/1.4974944
Submitted: 26 September 2016 • Accepted: 13 January 2017 • Published Online: 09 February 2017

Matjaž Panjan and André Anders

Plasma potential of a moving ionization zone in DC magnetron sputtering

Matjaž Panjan[1,2,a)] and André Anders[1,a)]
[1]*Lawrence Berkeley National Laboratory, 1 Cyclotron Road, MS 53, Berkeley, California 94720, USA*
[2]*Jožef Stefan Institute, Jamova 39, 1000 Ljubljana, Slovenia*

(Received 26 September 2016; accepted 13 January 2017; published online 9 February 2017)

Using movable emissive and floating probes, we determined the plasma and floating potentials of an ionization zone (spoke) in a direct current magnetron sputtering discharge. Measurements were recorded in a space and time resolved manner, which allowed us to make a three-dimensional representation of the plasma potential. From this information we could derive the related electric field, space charge, and the related spatial distribution of electron heating. The data reveal the existence of strong electric fields parallel and perpendicular to the target surface. The largest **E**-fields result from a double layer structure at the leading edge of the ionization zone. We suggest that the double layer plays a crucial role in the energization of electrons since electrons can gain several 10 eV of energy when crossing the double layer. We find sustained coupling between the potential structure, electron heating, and excitation and ionization processes as electrons drift over the magnetron target. The brightest region of an ionization zone is present right after the potential jump, where drifting electrons arrive and where most local electron heating occurs. The ionization zone intensity decays as electrons continue to drift in the $\mathbf{E}_z \times \mathbf{B}$ direction, losing energy by inelastic collisions; electrons become energized again as they cross the potential jump. This results in the elongated, arrowhead-like shape of the ionization zone. The ionization zone moves in the $-\mathbf{E}_z \times \mathbf{B}$ direction from which the to-be-heated electrons arrive and into which the heating region expands; the zone motion is dictated by the force of the local electric field on the ions at the leading edge of the ionization zone. We hypothesize that electron heating caused by the potential jump and physical processes associated with the double layer also apply to magnetrons at higher discharge power, including high power impulse magnetron sputtering. [http://dx.doi.org/10.1063/1.4974944]

I. INTRODUCTION

Magnetron sputtering (MS) is a physical vapor deposition technique commonly used in laboratory research and industrial practice for the fabrication of high-quality thin films and coatings. The technique has evolved from the simplest continuously running direct current (DC) regime, i.e., direct current magnetron sputtering (DCMS), to more complex oscillatory and pulsed regimes. Although oscillatory and pulsed modes, such as radio frequency magnetron sputtering (RFMS) and High Power Impulse Magnetron Sputtering (HiPIMS) are regularly used, the most common mode of magnetron operation is conventional DCMS.

Since the introduction of MS in the 1960s,[1] magnetron discharges have been extensively studied. A wealth of data about the properties of magnetron plasmas can be found in the literature.[2] Until the relatively recent discovery of rotating plasma structures[3–5] it was generally believed that the plasma density in the magnetron discharge is homogenously distributed in the region above the target's racetrack (the "racetrack" is the area of strongest target erosion caused by sputtering and determined by the electron drift path). Studies with fast cameras and different time-resolving plasma diagnostic techniques have changed this view. Imaging with intensified charge-coupled device cameras (ICCD cameras) at exposure times typically shorter than 1 μs revealed that plasma is concentrated in dense regions of well-defined shape. The terms *ionization zones* or *spokes* have been established for such plasma regions. The observed zones are strictly speaking zones of enhanced light emission, which is caused by inelastic collisions of electrons with the atoms and ions. The shape and position of the cross sections for excitation and ionization as functions of electron energy are similar. Therefore, zones of enhanced excitation are approximately also zones of enhanced ionization. The term "ionization zone" points to physical processes, while "spoke" is shorter and often used in the literature. We use "spokes" synonymously to "ionization zone," especially when making comparisons with the literature.

Ionization zones were first imaged in HiPIMS discharges[3–5] and later also in low-current DCMS discharges.[6,7] In both regimes, ionization zones are observed for a wide range of discharge conditions. Ionization zones are stochastic, evolving patterns which occasionally become periodic, indicating self-organization of magnetron plasma.[4–6] Conditions for stochastic versus regular patterns depend on many factors and have been explored in recent publications.[8,9] Generally, the pattern of ionization zones in DCMS tend to be periodic, which was one of the main reasons to utilize DCMS for the current study.

In DCMS, each ionization zone exhibits an elongated arrow-like shape with the tip pointing in the $\mathbf{E} \times \mathbf{B}$ direction. The number of ionization zones varies with working gas pressure. For a laboratory-sized magnetron, a single

a)Author to whom correspondence should be addressed. Electronic mail: matjaz.panjan@ijs.si, aanders@lbl.gov

ionization zone forms at very low gas pressures while the number of zones increases when the pressure is increased.[6] Symmetric patterns are commonly observed when two or more zones are present. In HiPIMS discharges, the zones are triangular at low pressure, having an arrow-like shape, with the tip pointing in the $\mathbf{E} \times \mathbf{B}$ direction, and more globular at higher pressure. Ionization zones in HiPIMS are typically shorter and more numerous than in the DC regime. HiPIMS ionization zones are more complex and dynamic. In HiPIMS discharges, the ionization zones move in the same direction as the $\mathbf{E} \times \mathbf{B}$ electron drift,[10] while in the low-current DCMS, discharge zones move in the opposite, i.e., to the $-\mathbf{E} \times \mathbf{B}$ direction.[11] Reversal in the direction of motion has been observed when varying the discharge current between the DCMS and HiPIMS regimes.[8,11] The velocity of ionization zones depends on the discharge conditions but is typically around 3–10 km/s, which is around one order of magnitude lower than the electron drift velocity.

Formation of highly non-uniform and non-stationary plasma in the magnetron discharges demonstrates that the plasma parameters, such as plasma density, plasma potential, electron temperature, and others, have a strong spatial and temporal dependence. Plasma potential distribution, which is a result of the space charge distribution, determines the transport and energy of electrons and ions. In the literature, several spatial measurements of the plasma potential can be found for different modes of magnetron operation. Plasma potential is most commonly evaluated from the *I-V* characteristics of Langmuir probe.[12–22] For DCMS discharges, plasma potential measurements were carried out at a single location,[18,20,22] in the axial direction at a fixed radial position[12–14] or in the radial direction at fixed axial locations.[15,16,19,21] Spatial mapping of plasma potential in the radial-axial plane was also carried out for DCMS discharge.[17] In HiPIMS discharges, the plasma potential has also been measured with the Langmuir probes.[23–25] More advanced measurements in HiPIMS have been conducted with the emissive probe technique to map the plasma potential in the radial-axial plane during the HiPIMS pulses.[26,27] Measurements of plasma potential for pulsed mid-frequency MS[28–30] and radio-frequency MS[31,32] are also available.

The literature provides plentiful information on plasma potential measurements in magnetron discharges. However, all conducted measurements were averaged over a longer time period (or over many pulses/oscillations), thus they could not capture any variations in the plasma potential associated with rotating ionization zones. Moreover, the Langmuir probe technique, which is most commonly used for the evaluation of the plasma potential, requires a finite time to record the *I-V* characteristic and thus cannot provide potential variations on a microsecond scale—a typical time scale related to the motion of zones. Several authors studied the temporal fluctuations in the *floating potential* and some associated it with the moving ionization zones.[8,33–37] Such measurements are relatively simple but offer a little insight into the properties of plasma since the motion of charged particles is affected by the gradient of the plasma potential and not by the gradient of the floating potential.

The goal of this work was to perform time- and space-dependent measurements of the plasma potential for a single, rotating ionization zone in the DCMS discharge. We used an emissive probe technique to record the time-dependent plasma potential in the radial and axial directions. From such measurements, we could reconstruct a full three-dimensional map of the plasma potential. The data captures the complete potential distribution in the radial and axial directions as well as in the azimuthal direction and thus provides an actual map of the plasma potential in DCMS discharge.

II. EXPERIMENTAL DETAILS

The experimental setup is schematically presented in Fig. 1. The experiments were conducted in a cylindrical vacuum chamber with 35 cm diameter and 25 cm height. The system was pumped to a base pressure below 10^{-4} Pa with a turbomolecular pump (Pfeiffer TMH 521) backed by a diaphragm pump (Vacuubrand). The working argon gas pressure was 0.27 Pa (2 mTorr) as recorded by a capacitance manometer (Baratron by MKS). An unbalanced planar magnetron (MeiVac Inc.) was used with a 76 mm (3 in.) diameter niobium target (thickness 6.25 mm). The anode ring was positioned around the target and mounted flush with the target surface avoiding any mechanical obstructions during the probe measurements. The magnetic field over the racetrack pointed from the target rim (magnetic north) to the target center (magnetic south). Detailed measurements of the magnetic field distribution can be found in Ref. 27. The discharge was operated by a DC power supply (Pinnacle from

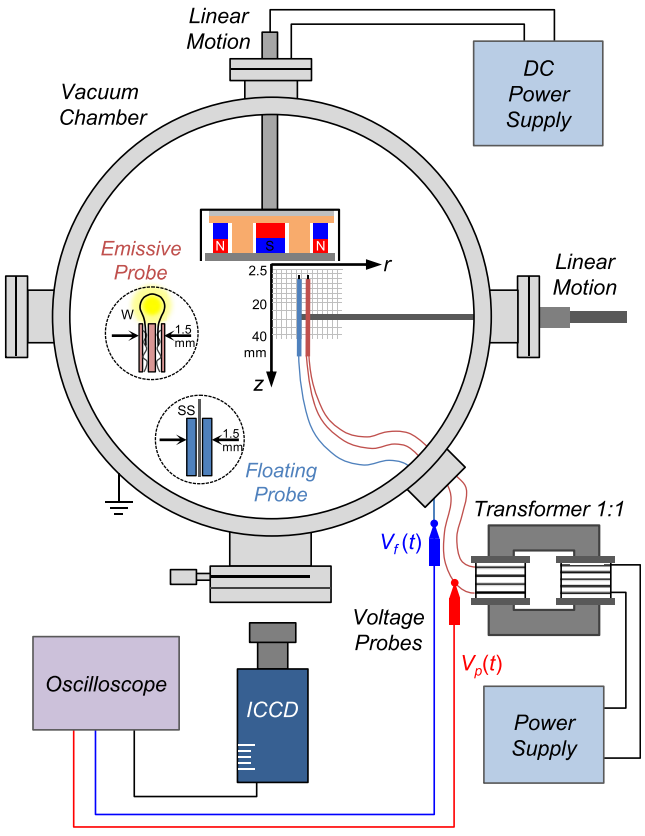

FIG. 1. Experimental setup for measuring the plasma and floating potentials.

Advanced Energy - maximum 1 kV, maximum 5 kW). Since the power supply was not capable of finely regulating the discharge current at very low currents (i.e., in the mA range) a separate current-limiting low-inductance resistor was added to enable the stable operation of the magnetron at very low currents while using the power supply in the voltage mode. All potential measurements were performed at discharge conditions which yielded a single rotating ionization zone; i.e., at a pressure of 0.27 Pa (argon) and a discharge current of 100 mA.

The emissive probe used in measurements was constructed from an alumina ceramic tube (diameter 1.5 mm) with two bored holes and contacts for the filament. A 50 μm diameter tungsten wire was pushed and fitted into the holes to form a semicircular loop with about 1 mm diameter as indicated in Fig. 1. The resistance between the connectors was less than 1 Ω, as determined by the tungsten loop, when the probe was cold. The probe was connected to a secondary coil of a transformer that induced heating of the filament while the primary coil was connected to an AC (60 Hz) power supply. The transformer enabled the decoupling of the probe's potential from the grounding of the heating power supply. About 2 V were needed to heat up the filament to large enough emissive current (further discussed in Sec. III A). The plasma potential was measured as the floating potential on the heated filament of the emissive probe. According to the emissive probe theory,[38] the floating potential of the heated filament reaches the plasma potential at sufficiently high heating currents when the flux of emitted electrons from the heated filament is equal to or larger than the flux of electrons from the plasma to the filament. The potential on the emissive probe was measured by a voltage probe (100×, Tektronix P5100). The probe signals were recorded by the data acquisition system PXI 5105 (National Instruments). A detailed description of the emissive probe technique can be found in Refs. 27 and 38.

In addition to the emissive probe, another, non-heated probe was inserted into the plasma to measure the floating potential. The probe was constructed from a stainless steel wire with a diameter of 0.5 mm inserted in a ceramic tube having 1.5 mm outer diameter. About 1 mm length of the wire was exposed to the plasma. The probe was located about 2 mm away from the emissive probe in the radial direction but at the same axial distance from the target surface. In this way, we could compare the time-dependent signals between the floating and plasma potentials at approximately the same location.

The two probes were mounted on a linear-motion feedthrough that was operated outside the chamber. The ceramic tubes of probes were aligned with the axial direction of the target and moved from $r = 0$ mm to $r = 39$ mm in 3 mm steps. The oscilloscope was set to record 100 μs long signals with 16 ns resolution, which typically captured two periods of ionization zone rotation over the racetrack. At each position, at least ten signals were recorded in steps of approximately 0.5 s, but not averaged. After the set of measurements in the radial direction was completed, the discharge was stopped and the axial position of the magnetron was changed by moving its holding shaft. The axial distance between the probe and the target was changed in the range from $z = 2.5$ mm to $z = 20$ mm in 2.5 mm steps, and in the range from $z = 20$ mm to $z = 40$ mm in 5 mm steps.

Measurements of the plasma and the floating potentials were correlated with images recorded by a fast-shutter ICCD camera (PI-MAX I from Princeton Instruments). The camera was mounted with a Nikkor 85 mm f/1.8 lens, and the camera exposure time was set to 1 μs to capture a single image of the ionization zone. Maximum camera gain and fully opened lens aperture were used in all experiments. Signals from the probes and the camera trigger were recorded using the oscilloscope in order to determine the exact correlation between the probe signals and the image of the ionization zone.

III. RESULTS

A. Time-resolved plasma and floating potentials

Experiments were conducted for the discharge conditions with a single ionization zone rotating in the $-\mathbf{E_z} \times \mathbf{B}$ direction (the $\mathbf{E_z}$ vector points in the direction of the target). A single ionization zone can be obtained when using a small magnetron at low working gas pressures and low discharge currents.[6,11] Our small magnetron was therefore operated at Ar pressure of 0.27 Pa and target potential of −270 V, which yielded 100 mA discharge current. To verify the presence and stability of a single ionization zone, the potential measurements were regularly compared with ICCD images. Throughout the whole experiment, only a single ionization zone was observed in the ICCD "snapshot" images, while the time-resolved plasma and floating potentials showed periodic signals with an approximately constant time period. Hence, the ionization zone was stable and moved along the racetrack with approximately a constant velocity.

Fig. 2 shows the typical time-dependent plasma potentials (V_p) and the floating potentials (V_f) that were recorded at several axial positions above the target. Measurements were performed in the high-density plasma region ($r = 24$ mm) above the target's erosion area, i.e., over the "racetrack" of the target. On the right axis of the graphs, the difference between the plasma and floating potentials ($V_p - V_f$) is presented (such signal is related to the energization of electrons and is discussed in Section III E). In all recorded data, a periodic signal with approximately two periods is visible (i.e., two rotations of the ionization zone). Measurements performed at each location were reproduced with high fidelity: there was less than 5% variation in the amplitude of the signals. The reproducibility of signals is demonstrated in the supplementary material S1.

It should also be emphasized that probes did not significantly disturb the discharge even when measuring at the closest distance from the target ($z = 2.5$ mm). The applied voltage was slightly adjusted for each position of the probes in order to maintain the 100 mA discharge current. In the supplementary material S2, we show variations in the target potential as a function of the probes' position. Even when measuring at the closest distance from the target ($z = 2.5$ mm), the target voltage had to be adjusted only by about 5%, namely, from −265 V when the probe was in the center of magnetron to −280 V when the probe was over the

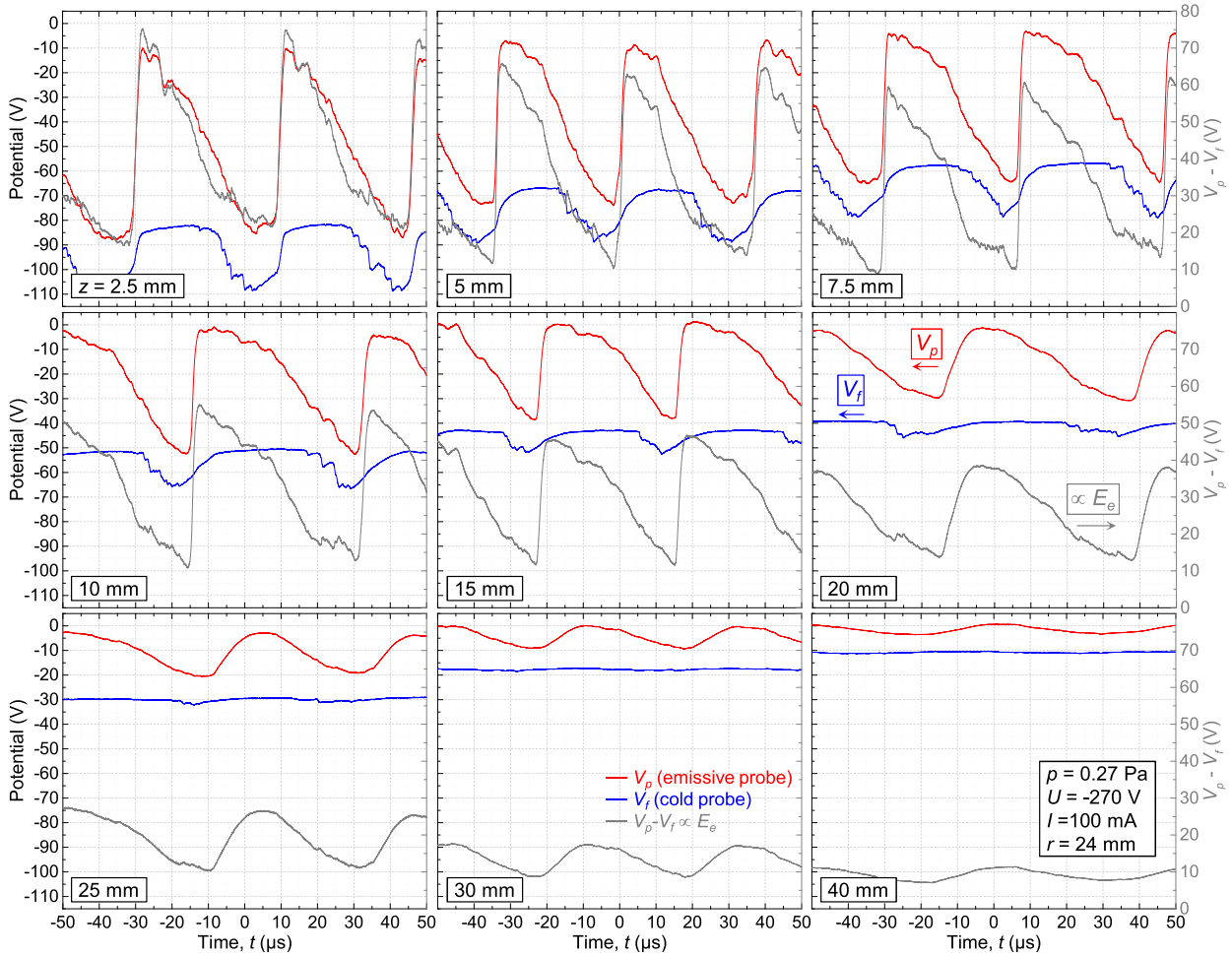

FIG. 2. Plasma potential (V_p, red curve) and floating potential (V_f, blue curve) recorded at $r = 24$ mm and different axial distances from the surface of the target ($z = 2.5$–40 mm). Right axis shows the difference between the plasma and the floating potentials, V_p - V_f (gray curve), which is proportional to the energy of the electrons. Reproducibility of the signals is demonstrated in the supplementary material S1.

racetrack region. When the probe was further away from the target, the target voltage had to be adjusted only by a few volts. Based on these data, we conclude that the probes did not significantly alter the discharge even when conducting measurements very close to the target. Moreover, the ICCD images showed only the arrowhead-like shape of the ionization zone, and the potential measurements displayed periodic signals.

The time periods of the plasma and the floating potentials are approximately the same showing that the ionization zone takes 35–45 μs to travel once around the closed racetrack (Fig. 2). The plasma and floating potentials have different curve shapes. Looking from the most negative potential value, the plasma potential increases sharply to a maximum value close to 0 V and then decreases in a parabolic-like shape to the initial potential value. For the floating potential, a different characteristic curve shape is observed. The floating potential increases slower, resembling an S-curve, reaches a plateau, and then decreases in a series of steps towards the initial potential value. The amplitudes of the floating and plasma potentials are different. For example, at $z = 2.5$ mm, the amplitude of the plasma potential varies between -85 V and -10 V, whereas the values of the floating potential are more negative, ranging from approximately -110 V to -85 V. The plasma potential becomes less negative as the axial distance is increased, e.g., from $V_{p,min} = -85$ V at $z = 2.5$ mm to $V_{p,min} = -5$ V at $z = 40$ mm. On the other hand, the maximum values of the plasma potential increase only slightly, e.g., from $V_{p,max} = -10$ V at $z = 2.5$ mm to $V_{p,max} = 0$ V at $z = 40$ mm. Hence, the plasma potential approaches the ground potential at larger axial distances. In the case of the floating potential, the minimum potential values change from $V_{f,min} = -110$ V at $z = 2.5$ mm to $V_{f,min} = -10$ V at $z = 40$ mm, whereas the maximum values change from $V_{f,max} = -82$ V at $z = 2.5$ mm to $V_{f,max} = -11$ V at $z = 40$ mm; i.e., the signal shifts towards the ground potential. Although the amplitudes of the plasma and floating potentials decrease with increasing axial distance from the target, the characteristic shape of the signals stays more-or-less the same.

Supplementary material S3 shows the floating potential of the emissive probe as a function of filament heating current for a fixed probe position. The amplitude of the potential is small when heating current is less than 1 A but reaches largest and stable values when the heating current is greater than 1.3 A; Most importantly: the potential does not change with further increase of the heating current. Hence, it can be assumed that the potential on the filament heated with at

least 1.3 A "floated" to the plasma potential. To ensure large-enough filament heating and electron emission, all measurements were conducted with a heating current exceeding 1.4 A.

The curves of $V_p - V_f$ show a similar shape as the curves of the plasma potential. However, the values of $V_p - V_f$ are positive (see right axis of Fig. 2) since the floating potential is always more negative than the plasma potential. The amplitude of $V_p - V_f$ decreases with the increasing distance from the target in a similar manner as in the case of the plasma potential. The maximum values of $V_p - V_f$ also decrease and approach 10 V at $z = 40$ mm distance.

Potential measurements at different radial positions and fixed axial distance ($z = 5$ mm) are shown in Fig. 3. Similar shapes of the potential curves can be distinguished as in the curves in Fig. 2. However, the amplitudes of the curves change in a different manner. Close to the center of the magnetron ($r = 9$ mm) and close to the outer perimeter of the magnetron ($r = 33$ mm) only small variations in the amplitude are observed, while over the race-track region ($r = 15$–27 mm) large fluctuations in the potentials are present. Hence, the plasma and floating potential change from the near-ground potential in the center of the magnetron, to large potential variations over the racetrack area, and then again toward the ground potential when approaching the anode.

In the signals of the plasma and floating potentials, finer structures can be observed. This is particularly visible for measurements performed near the target and above the race-track area. In the case of the plasma potential, one can observe oscillations after a sharp increase in the potential, while in the floating potential, a pronounced series of steps are visible towards the end of the period (i.e., after the flat part of the curve).

B. Correlation between potential measurements and fast camera images

The plasma and floating potentials were correlated with the light distribution of the ionization zone as recorded by the ICCD camera. Fig. 4 shows examples of three images and corresponding potential measurements recorded at different axial distances from the target surface ($z = 5$, 10, 15 mm). The emissive and the floating probes were located radially at $r = 21$ mm, while the angular position was at approximately 0° azimuthal angle (the bright spot at 0° originates from the heated filament of the emissive probe). The contrast of the image was non-linearly enhanced (gamma correction) to increase the faint light of the ionization zone

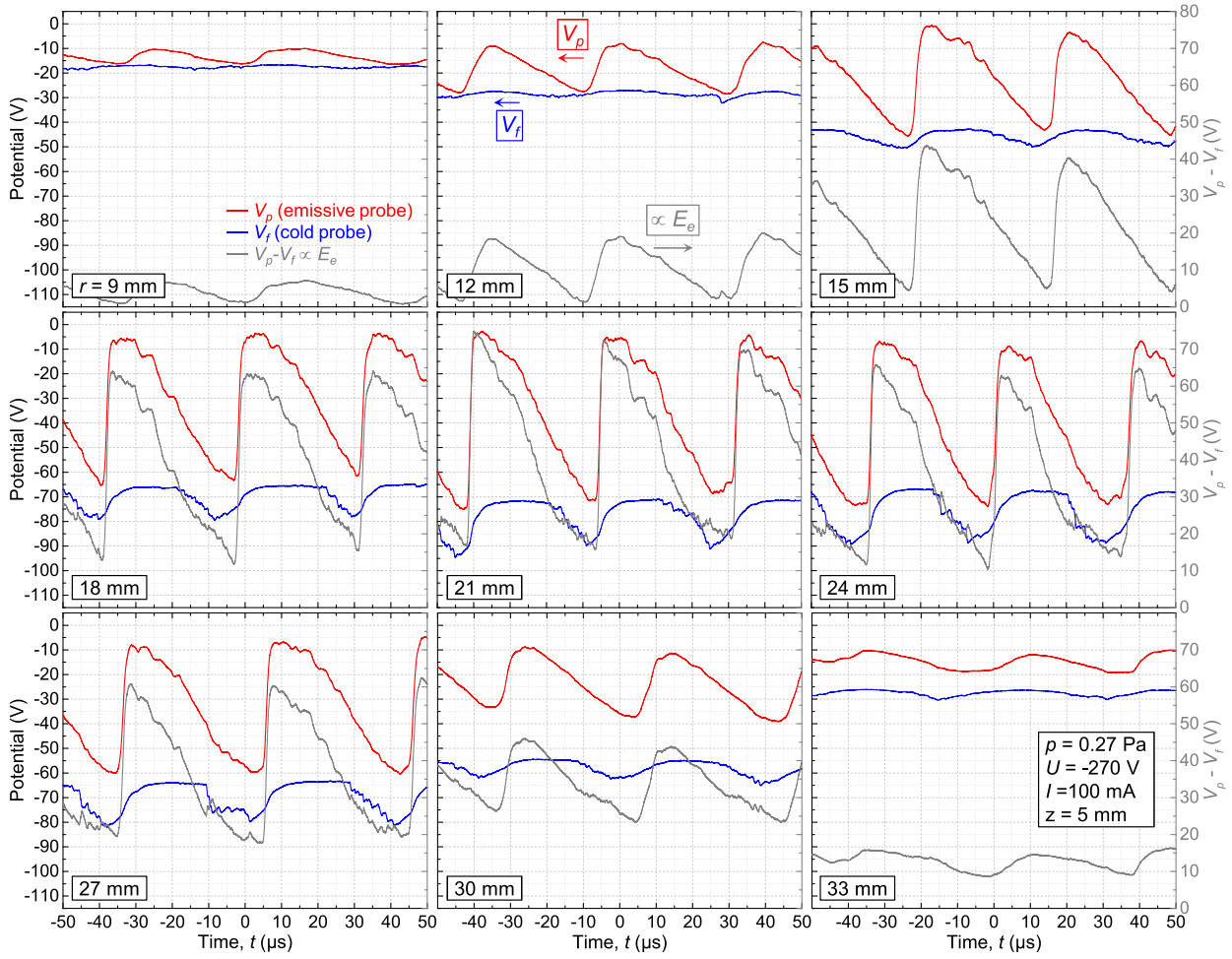

FIG. 3. Plasma potential (V_p, red curve) and floating potential (V_f, blue curve) measured at $z = 5$ mm and different radial distances from the center of the magnetron ($r = 9$–33 mm). Right axis shows the difference between the plasma and the floating potentials, V_p - V_f (gray curve), which is proportional to the energy of the electrons.

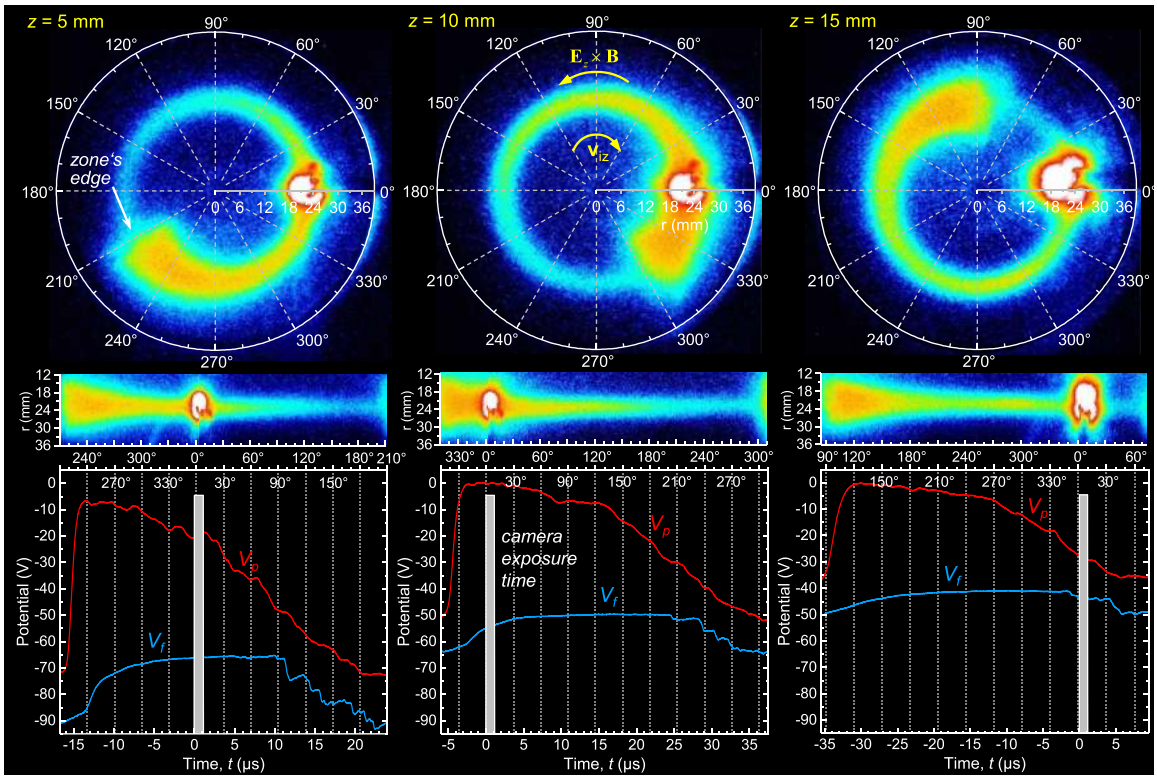

FIG. 4. Correlation between the emitted light (ICCD images, false color indicates intensity) and potential measurements (probes were positioned at $r = 21$ mm). The middle images were mathematically transformed into a linear light distribution for ease of presenting the correlation. The bright spot at 0° originates from the light emitted by the heated filament of the emissive probe. The direction of ionization zone motion is clock-wise, the $-\mathbf{E} \times \mathbf{B}$ direction. Contrast of the image was non-linearly enhanced (gamma correction) in order to increase the faint light intensity of the ionization zone as compared with the intensity of the bright filament.

in comparison to the bright light of the filament. Due to non-linear enhancement, the bright spot is saturated and appears excessively large. The spatial light distribution was mathematically transformed from polar to linear coordinates (middle images in Fig. 4) to establish more easily the correlation between images and the measured time-dependent potentials.

Images from the ICCD camera shown in Fig. 4 demonstrate that the most negative potential values (both for the plasma and the floating potential) are correlated with the leading edge of the ionization zone. Hence, the bright edge of the zone is related with the sharp increase in the plasma potential. In the region of the highest light intensity, just after the edge of the zone, the plasma potential reaches potential values near the ground potential. The ionization zone is associated with a potential structure which has a shape of a potential hump, as was inferred in Ref. 39. The floating potential correlates with the ICCD images in a similar way; i.e., the minimum of the floating potential is correlated with the edge of the ionization zone although the increase in the floating potential near the zone's edge is slower than the increase in the plasma potential.

C. Spatial distribution of plasma potential and electric field

Measurements recorded at different axial and radial positions, presented in Section III A, were combined to reconstruct the full three-dimensional distributions of the plasma potential and of the electric field. For visualization of the spatial distributions, the time-dependent plasma potentials (such as in Figs. 2 and 3) were first converted into angular coordinate by normalizing single periods in the angles between 0° and 360°. The electric field was then calculated from the plasma potential

$$\mathbf{E} = -\nabla V_p. \tag{1}$$

In the cylindrical coordinate system, i.e., $V_p(r, \xi, z)$, the electric field components are

$$\mathbf{E} = (E_r, E_\xi, E_z) = -\left(\frac{\partial V_p}{\partial r}, \frac{1}{r}\frac{\partial V_p}{\partial \xi}, \frac{\partial V_p}{\partial z}\right). \tag{2}$$

In Fig. 5 the plasma potential and the electric field distributions are presented in the azimuthal-radial plane (ξ-r) for the different axial distances. Distributions are shown from $z = 2.5$ mm (the measurement closest to the target) to $z = 40$ mm (the furthest distance from the target surface). Along with the potential measurements, an image of ionization zone is shown whose angular position approximately corresponds to the measured potential distributions.

In the azimuthal direction, a large potential difference can be observed around the edge of the ionization zone (i.e., $\xi \approx 20°$–$30°$ in the example of Fig. 5). The highest plasma potential values (i.e., around 0 V) are found after the edge of the ionization zone where the light intensity and plasma

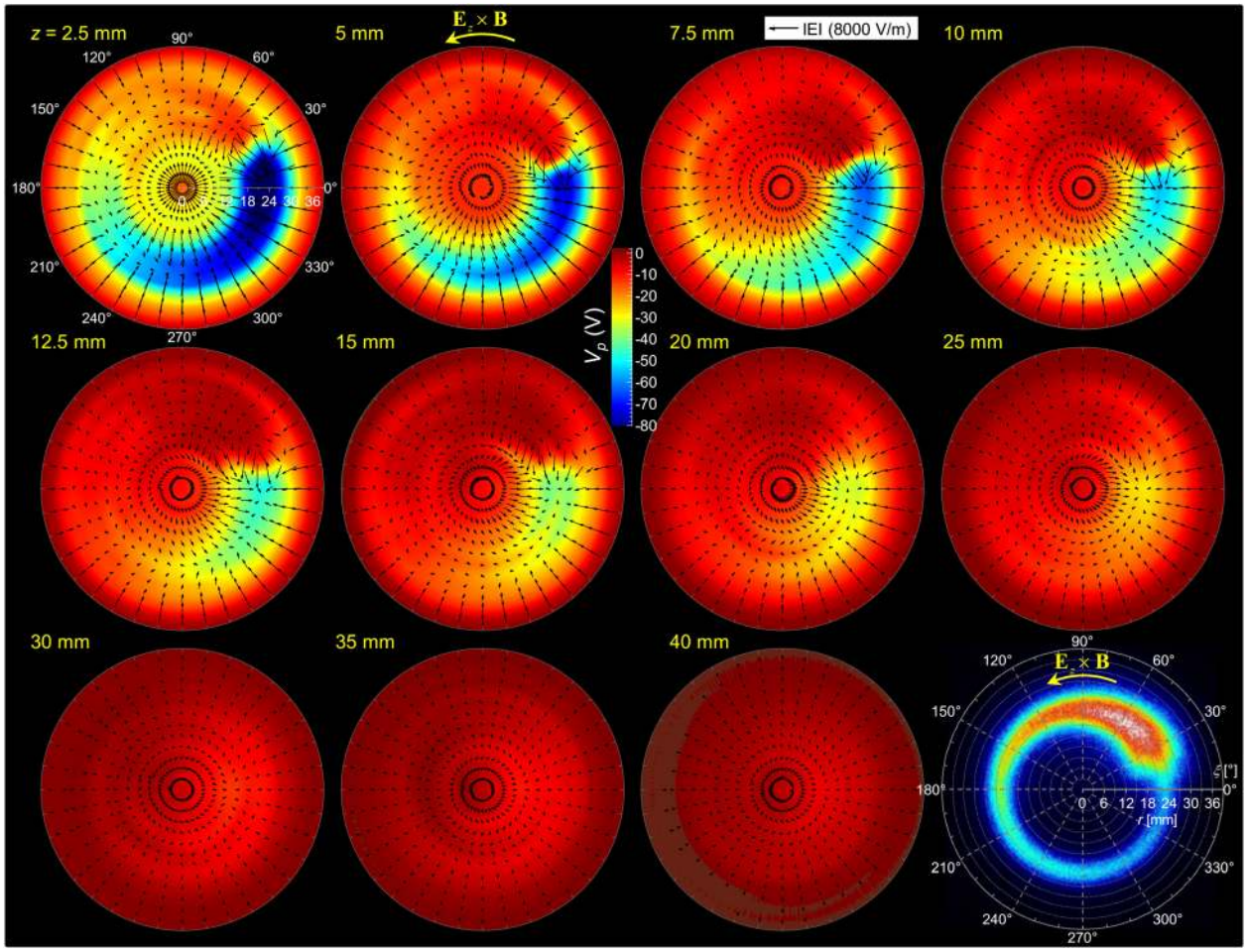

FIG. 5. Plasma potential (color) and electric field (vector) distributions in the ξ-r plane for different axial distances from the target surface ($z = 2.5$–40 mm). The ICCD image of the ionization zone on the bottom right approximately corresponds to the measured plasma potential distribution. Measurements were performed for the pressure of 0.27 Pa, target potential of -270 V, and a discharge current of 100 mA.

density are the highest. Here we use terms "after" and "before the edge of the zone" in relation to the direction of the azimuthal coordinate from the point of view of drifting electrons: "before" means a location before electrons arrive at the leading edge of the ionization zone, and "after" is when they have passed it. This terminology is unambiguous and applicable to all magnetrons since the electron drift is in the $\mathbf{E}_z \times \mathbf{B}$ direction and always faster than the motion of an ionization zone.

Looking at the azimuthal potential distribution before the edge of the ionization zone, where the intensity of the light and plasma density are the lowest, the plasma potential reaches the most negative values; e.g., -90 V for measurement at $z = 2.5$ mm. At larger axial distances (greater z), the jump in the plasma potential at the edge of the zone becomes smaller but is still significant. For example, 10 mm above the target ($z = 10$ mm), the difference in the potential is around 50 V, whereas at $z = 20$ mm, the difference is around 30 V. For measurements close to the target, one can see that the ionization zone is associated with the potential distribution in the shape of *potential hump*.

In the radial direction, considerable variations in the plasma potential can also be observed. Variations depend on the azimuthal position. In the low-light region, e.g., $\xi = 270°$–$360°$ in the example of Fig. 5, the plasma potential goes from the near-ground potential in the center of the magnetron to large negative potentials (e.g., -90 V at $z = 2.5$ mm) and back to near-ground potential close to the anode (i.e., $r \sim 40$ mm). However, in the region of high light intensity (e.g., $\xi = 30°$–$90°$), the spatial distribution of the potential is significantly different; namely, the plasma potential over the racetrack area is several volts higher than the potential in the center of the magnetron and close to the anode.

Potential gradients in the azimuthal and radial directions represent in-plane electric fields. The strongest electric fields form at the edge of the ionization zone and point in the $-\mathbf{E}_z \times \mathbf{B}$ direction. At $z = 2.5$ mm, the electric field strengths reach up to 10 kV/m. Further away from the target; e.g., at $z = 10$ mm, the electric field strength is still strong with values of around 5 kV/m. Although these fields are weaker than the axial electric fields in the sheath/pre-sheath region (estimated to be on the order of 100 kV/m), they have significant strengths that can strongly affect the motion of electrons and ions.

In the radial direction, relatively large electric fields are also present. Their strengths and directions depend on the azimuthal position. In the low-density plasma region of the ionization zone (e.g., $\xi = 270°$–$360°$ in the example of Fig. 5), the electric fields are directed toward the racetrack

region and reach strengths up to 5 kV/m (at $z = 2.5$ mm), while in the high-density plasma region (e.g., $\xi = 30°$–$90°$), the electric fields point radially away from the racetrack region (the fields are weaker, e.g., 1–2 kV/m at $z = 2.5$ mm). At larger distances from the target surface, the in-plane electric fields become smaller and practically disappear at distances larger than 30 mm.

A radial view of the plasma potential and the electric field is presented in Fig. 6. The figure shows distributions in the ξ-z plane for different radial positions. The sharp edge of the plasma potential at approximately $\xi = 20°$–$30°$ corresponds to the leading edge of the ionization zone. The edge is most pronounced over the racetrack area (i.e., $r = 15$–27 mm). In the area of the ionization zone where the intensity of the light is the highest (i.e., $r = 15$–27 mm and $\xi = 30°$–$120°$), the potential changes from −270 V (potential at the target surface) to −10 V over a distance of approximately 3 mm, while in the area of low-light intensity (i.e., $r = 15$–27 mm and $\xi = 300°$–$360°$), the same potential difference occurs over a distance of approximately 30 mm. Hence, the plasma potential in the axial direction strongly depends on the position along the azimuthal direction (particularly over the racetrack area).

Steep potential gradients represent strong electric fields: they are present at the edge of the ionization zone and point in the $-\mathbf{E_z} \times \mathbf{B}$ direction. Over the racetrack area and close to the target, a strong electric field on the order of 10 kV/m is inclined towards the target. The plasma potential is locally higher in the region of the highest light intensity (see dark red area for $\xi = 30°$–$120°$ and z = 5–20 mm), which results in the electric field vectors pointing away from this region.

Another representation of the plasma potential and electric field distributions is shown Fig. 7. The figure presents a cross-sectional view through a radial-axial plane for different azimuthal angles. A more detailed distribution is presented in the supplementary materials S4 and S5. In the low-density plasma region ($\xi = 270°$–$360°$ in the example of Fig. 5), the electric field funnels ions towards the racetrack area. A strong radial component of the electric field can be observed up to 20 mm above the target. In contrast, in the region of the high-density plasma ($\xi = 30°$–$90°$), the electric field lines point away from this region. Electric field vectors point radially away from the high density region, toward the target and also axially away from the target.

D. Space charge distribution

The distribution of the plasma potential is determined by the spatial distribution of the charged particles. Gauss' law relates space charge (ρ) with the electric field, while in

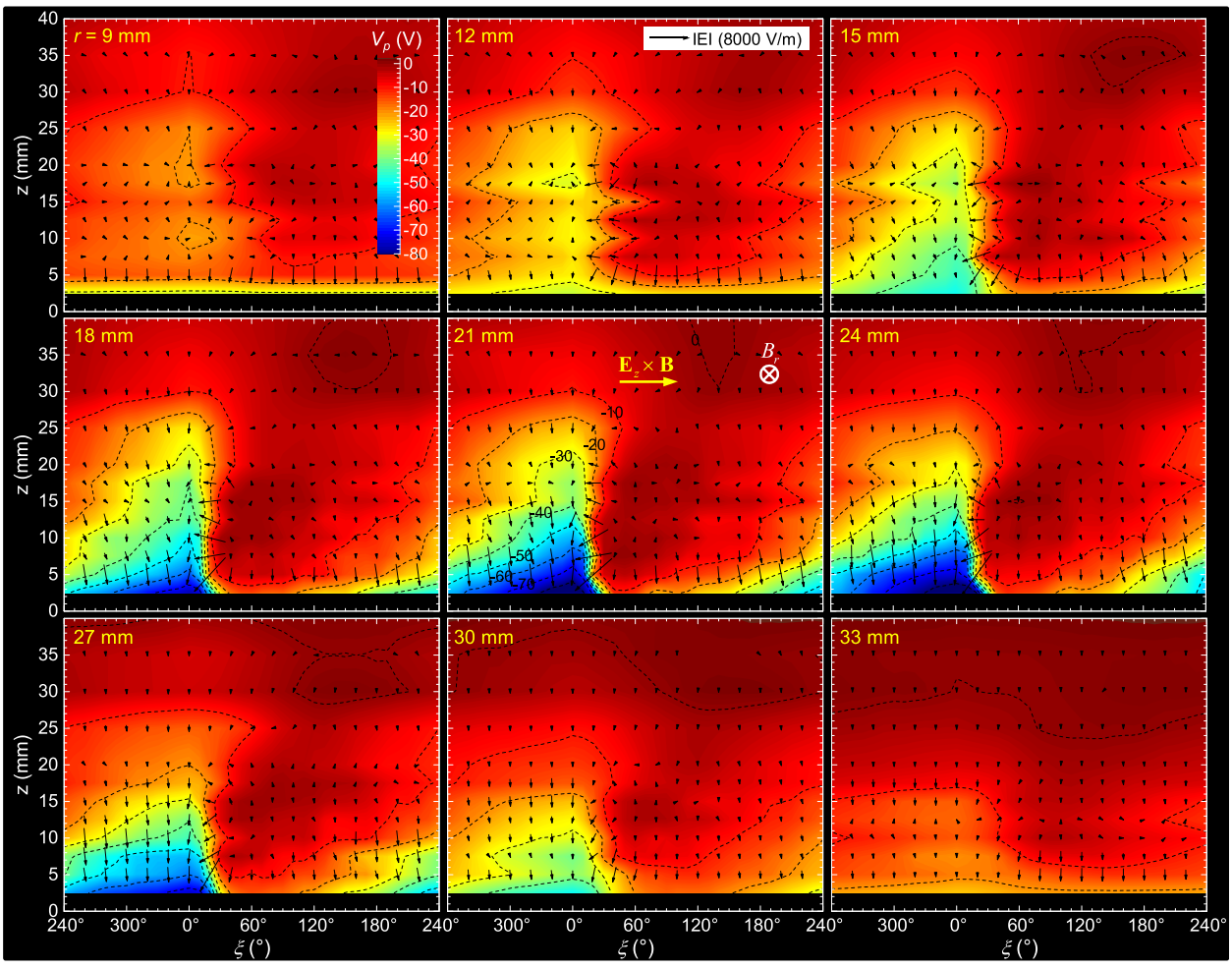

FIG. 6. Plasma potential (color) and electric field (vector) distributions in the ξ-z plane presented for different radial positions. The target is at $z = 0$, and ξ is the azimuthal coordinate (along the racetrack).

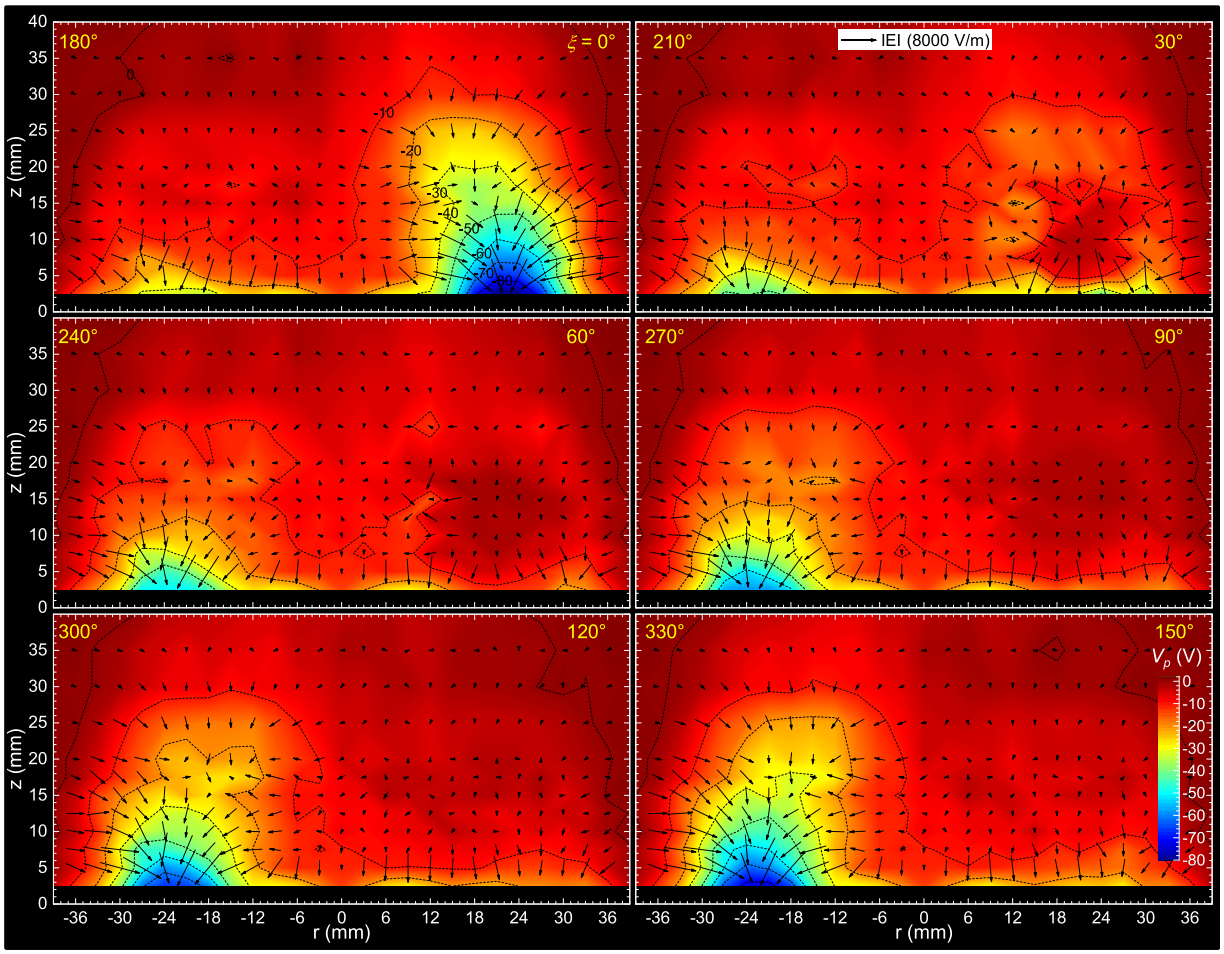

FIG. 7. Plasma potential (color) and electric field (vector) distributions in the r-z plane of the magnetron for different azimuthal angles (from $\xi = 0°$ to $\xi = 330°$ in steps of 30°). A more detailed presentation of the distribution can be found in the supplementary materials S4 and S5.

the Poisson equation, space charge is related directly to the plasma potential

$$\rho = \nabla \cdot \mathbf{E} = -\varepsilon_0 \nabla^2 V_p, \tag{3}$$

where ε_0 is the vacuum permittivity. In cylindrical coordinates, the Poisson equation is

$$\rho(r, \xi, z) = -\varepsilon_0 \left(\frac{\partial^2 V_p}{\partial r^2} + \frac{1}{r}\frac{\partial V_p}{\partial r} + \frac{1}{r^2}\frac{\partial^2 V_p}{\partial \xi^2} + \frac{\partial^2 V_p}{\partial z^2} \right). \tag{4}$$

The space charge is defined as

$$\rho = e(\bar{Q} n_i - n_e), \tag{5}$$

where e is the elementary charge, $\bar{Q}$ is the mean ion charge state number, n_i is ion density and n_e is electron density. For the low-current DCMS discharge, $\bar{Q} \approx 1$ (i.e., the concentrations of doubly or higher charged ions are negligible), therefore, in our case, the space charge represents the difference between the ion and electron densities, i.e., $\rho = e(n_i - n_e)$.

Fig. 8 shows the distribution of $n_i - n_e$ in the azimuthal-radial plane (r-z) measured at different axial distances from the target as it was calculated from Eqs. (3) and (5). Around the edge of the ionization zone (i.e., $\xi = 20°$–$30°$ in the example of Figs. 5 and 8), two regions of charge density are present. The red region represents locally higher ion density, while the blue region represents locally higher electron density. Such a structure of opposite electrical charge is often referred to as a *double layer*. In these two areas, the local difference between the ion and electron densities is on the order of $10^{14}\,\mathrm{m}^{-3}$. Such densities represent only about 1% of typical plasma densities found in DCMS discharges—those are on the order of $10^{16}\,\mathrm{m}^{-3}$.[12,15–17] The separation of the charge particles around the edge of the ionization zone is strong up to 10 mm away and then disappears at larger distances from the target. A region of increasingly negative space charge extends behind the edge of the ionization zone and over the racetrack area (see blue region for $\xi = 240°$–$360°$ at $z = 2.5$–7.5 mm). This region of locally higher electron density is responsible for the formation of radially directed electric fields (cf. Figs. 5 and 7). Away from the racetrack area, the plasma is quasi-neutral as represented by green color.

Fig. 9 shows a view of the $n_i - n_e$ distribution in the ξ-z plane. In this view, a local separation of ion and electron densities is visible around the edge of the ionization zone particularly for the radial positions $r = 18$–24 mm. The double layer near the edge of the ionization zone extends up to 15 mm away from the target surface. An increased electron density extends before the edge of the ionization zone up to $\xi = 240°$ and about $z = 7.5$ mm, which is most clearly visible

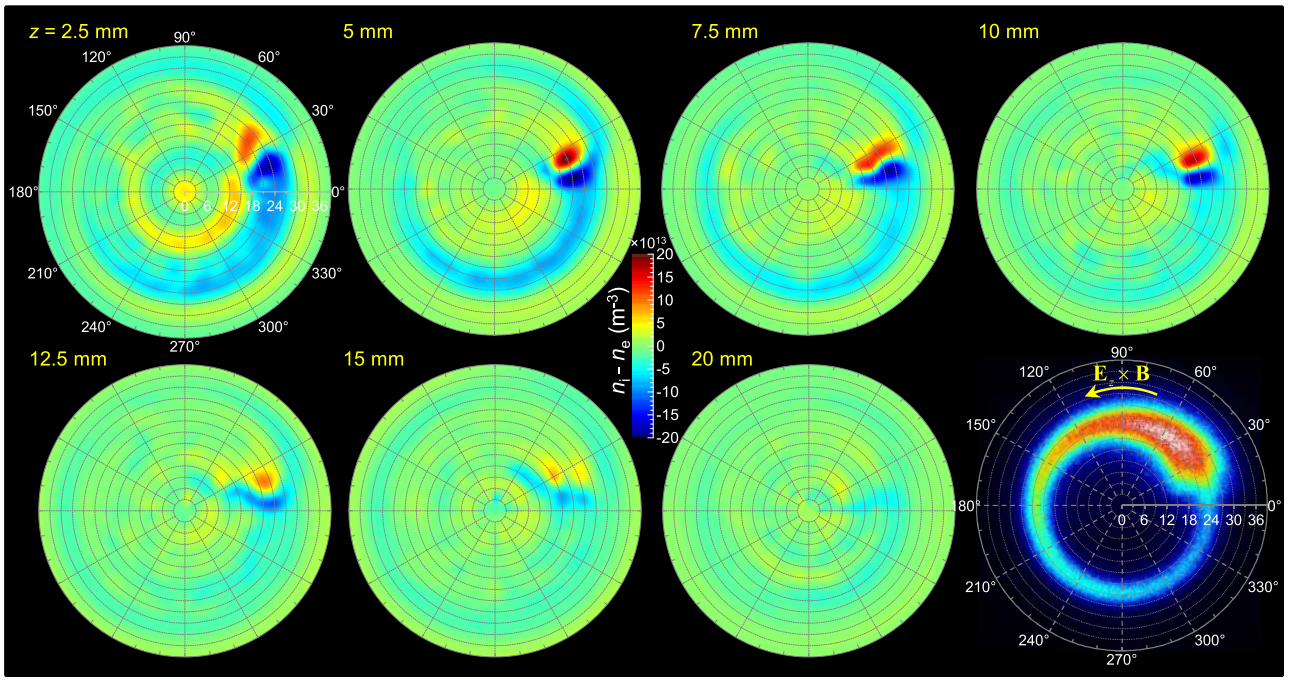

FIG. 8. Distribution of $n_i - n_e$ in the ξ-r plane for different axial distances from the target ($z = 2.5$–20 mm). Red areas represent a locally higher ion density, while the blue areas represent a locally higher electron density. In the area represented by green color, the plasma is quasi-neutral.

at $r = 24$ mm. Outside the racetrack region (i.e., from $r = 12$–15 mm), the ion density behind the edge of the ionization zone is slightly higher (yellow area); this causes radially directed electric fields. At the axial distances above 25 mm, the plasma is quasi-neutral (areas of green color).

E. Spatial distribution of electron energy

The plasma and floating potentials, which were recorded simultaneously at approximately the same spatial location, yield additional information on the properties of the plasma. The following expression holds for electrons with the Maxwellian energy distribution[38,40,41]

$$V_p - V_f = \frac{\ln(I_{es}/I_{is})}{\bar{Q}e} kT_e, \tag{6}$$

where T_e is the electron temperature, k is the Boltzmann constant, I_{es} is the electron saturation current, and I_{is} is the ion saturation current.

According to Eq. (6), the temperature of electrons is directly proportional to the difference between the plasma

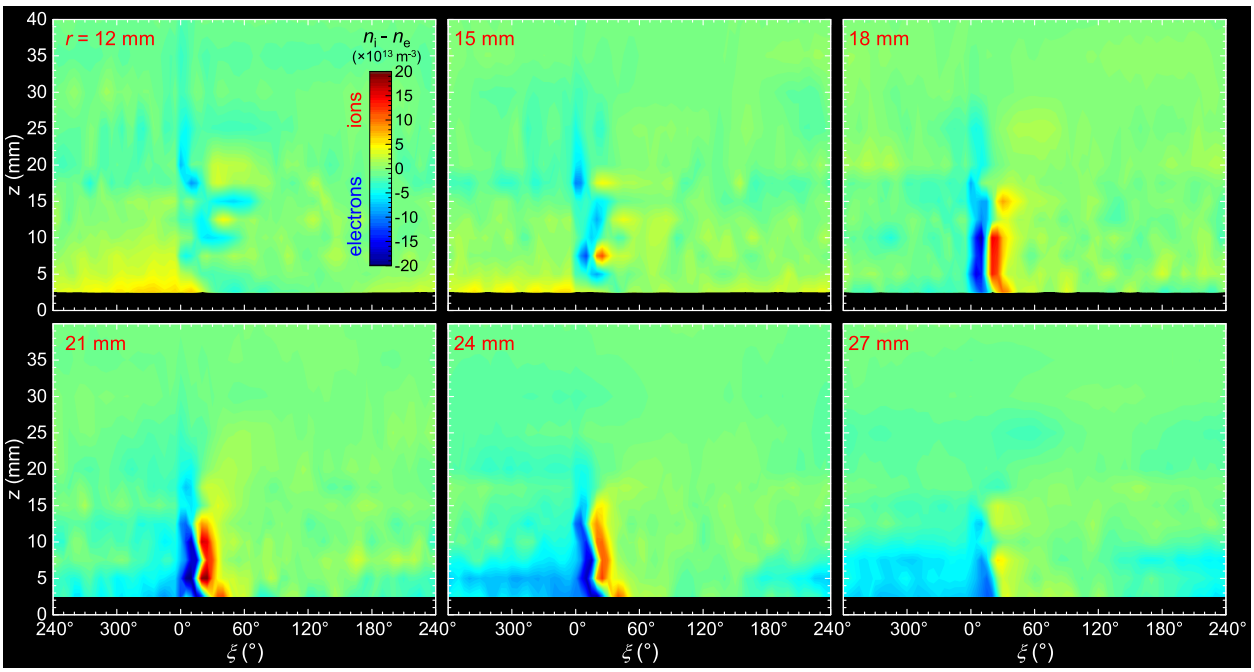

FIG. 9. Distributions of the net charge $n_i - n_e$ in the ξ-z plane presented for different radial positions.

potential and the floating potential ($kT_e \propto V_p - V_f$); the remaining factor is constant if the ratio between the electron and ion saturation currents is independent of the probe's position. This is true when probing quasineutral plasma but not when probing a space charge region. However, in the here-considered space charge regions of the presheath, the net charge density is much smaller than the absolute charge density, and therefore the ratio between the electron and ion saturation currents is only weakly affected. Further justification for neglecting changes in this factor is its logarithmic dependence on that ratio, which makes variations very weak.

Since the electron energy distribution in the magnetron discharges deviates significantly from a Maxwellian distribution[12,42] we will consider that the difference between the plasma and floating potential is proportional to a more general parameter related to the characteristic energy of electrons, i.e., $V_p - V_f \propto \langle E \rangle$. Much insight about the energy of electrons can be obtained by examining the spatial distribution of $V_p - V_f$.

Fig. 10 shows the spatial distribution of $V_p - V_f$ measured in the ξ-r plane for different axial distances from the target surface ($z = 2.5$–40 mm). The $V_p - V_f$ difference is positive for all measurements as expected from the fact that the energy of electrons can be only positive. A larger potential difference is correlated with locally higher electron energy. The red color in Fig. 10 represents the region of high-energy electrons ("hot electrons"), whereas the blue color represents the region of low-energy electrons ("cold electrons"). The distribution of $V_p - V_f$ shows that electrons have the highest energies in the magnetic trap region,[43] i.e., over the racetrack area. The highest energies can be observed just after the edge of the ionization zone and close to the target surface. The energy of electrons then decreases in the direction of the electron drift (the $\mathbf{E}_z \times \mathbf{B}$ direction) forming the same elongated arrowhead shape as the light intensity of the ionization zone. Hence, the light intensity of the ionization zone can be directly correlated with the spatial distribution of electron energy (compare the ionization zone image in Fig. 10 with the $V_p - V_f$ distributions). Electron energy also changes in the radial direction. In the magnetic trap, electrons have the highest energies, while those outside the magnetic trap have the lowest energies.

Measurements shown in Fig. 10 suggest that electrons drifting in the magnetic trap in the anticlockwise direction, lose a significant part of their energy. At $z = 2.5$ mm the energy of electrons just after the edge of the ionization zone is about four times higher than the energy of electrons just before the edge. This difference becomes smaller further

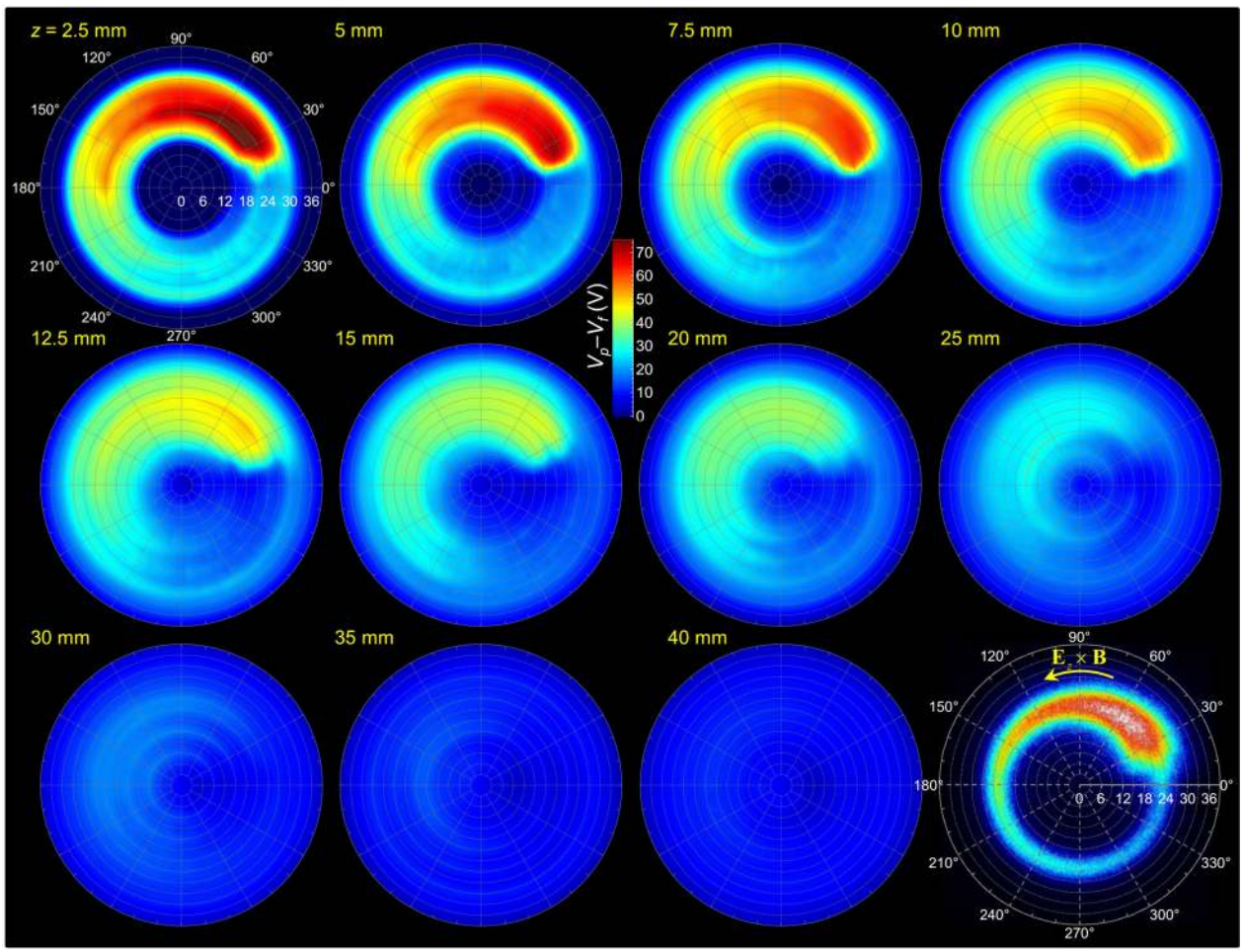

FIG. 10. Distribution of difference between the plasma potential and floating potential ($V_p - V_f$) measured in the ξ-r plane for different axial distances from the target surface ($z = 2.5$–40 mm). $V_p - V_f$ is related to the energy of electrons. The ICCD image of the ionization zone on the bottom right approximately corresponds to the measured $V_p - V_f$.

away from the target surface since the overall energy of the electrons decreases. In the center of the target surface and on the perimeter (close to the anode), the electrons have the lowest energies.

A view of the $V_p - V_f$ distributions in the ξ-z plane for several radial positions is shown in Fig. 11. From this perspective, it is clearly visible that over the central part of the racetrack ($r = 18$–24 mm), the electron energy is the highest; especially after the edge of the ionization zone and close to the target surface. The energy then decreases along the ionization zone in the $\mathbf{E}_z \times \mathbf{B}$ direction and further away from the target. However, higher energy electrons (e.g., $V_p - V_f > 40$ V) can be found even 15–20 mm away from the target surface and quite far azimuthally after the edge of the ionization zone (e.g., 120° after the edge of zone). On the other hand, low energy electrons are present near the edges of the racetrack (i.e., $r = 15$ mm and $r = 30$ mm). Additional presentations of the $V_p - V_f$ distributions in the r-z plane for different azimuthal angles are presented in the supplementary materials S6 and S7.

IV. DISCUSSION

A. Motivation for measuring time- and space-resolved plasma potential in DCMS

Direct current magnetron discharges are generally considered stationary and therefore most measurements found in the literature are not time resolved. In contrast, time-resolved measurements are performed for pulsed discharges, however, they are usually averaged over several pulses to improve the signal to noise ratio. Averaged potential distribution measurements using an emissive probe were done both for DCMS discharges,[17] and for HiPIMS discharges.[26,27,44] The combination of time- and space-resolved measurements, not exploited in previous studies,[27,44] are central to the work reported here. The objective of this work was to map the plasma and floating potentials in a space and time resolved manner, giving us the opportunity to answer the question whether the ionization zone is related to a simplified potential structure proposed in Ref. 45 or to a potential hump proposed in Ref. 39. The measurements of potential distribution together with obtained electric field, space charge, and electron energization distributions presented in this work therefore provide a greater insight into the dynamics, sustainability, and mechanism of localized electron heating[46] in moving ionization zones.

The choice of investigating the ionization zones in DCMS offers a great advantage as opposed to the investigating zones in HiPIMS. Namely, DCMS discharge can be adjusted to form only a single ionization zone, which travels with a constant speed and shape, making investigations relatively easy. In contrast, there are several traveling ionization zones in HiPIMS discharges affecting each other (self-organization)[5,47] and growing/decaying in a more-or-less chaotic manner producing different ionization zone patterns from pulse to pulse.[9] We therefore focused here on DCMS discharges and anticipate that the findings will provide much insight when interpreting the more complicated case of HiPIMS discharges.[48,49]

B. Double layer, potential hump, and electron energization

The existence of double layers is a well documented phenomenon for a wide range of magnetized plasmas studied both in space and laboratory environments.[50,51] Our measurements of the plasma potential (Figs. 5 and 6) also demonstrate the existence of a pronounced electric double layer (Figs. 8 and 9) in which the plasma potential jumps to much

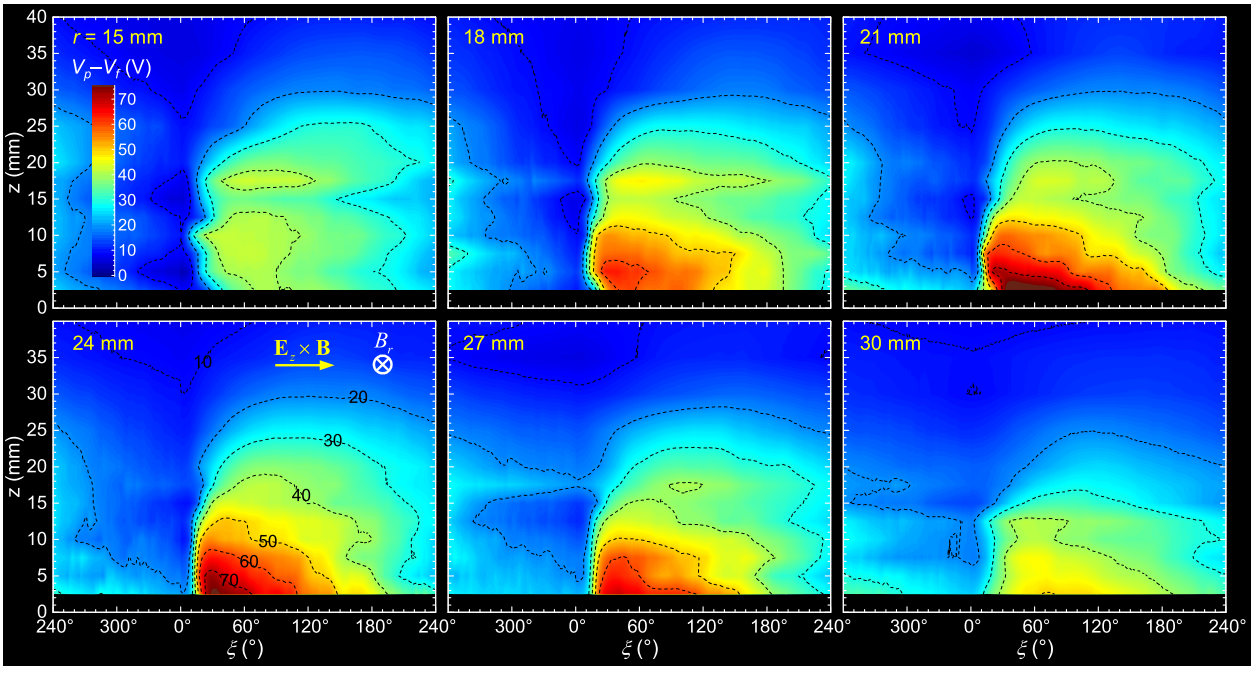

FIG. 11. Distribution of $V_p - V_f$ in the ξ-z plane presented for different radial positions. Distribution in the r-z plane is also presented in the supplementary materials S6 and S7.

higher values. After the potential jump, a potential hump extends in the $\mathbf{E}_z \times \mathbf{B}$ direction. We remind the reader that the term "after" to be understood from an electron drift direction point of view: "after" means the electrons have passed the double layer (i.e., potential jump). The hump is very asymmetric: it is steeply rising at the front and gradually decaying afterwards (much more asymmetric than anticipated in the schematic of Fig. 3(d) of Ref. 39).

Localized electron heating occurs whenever electrons go from lower to higher potential, either through collisions or via a collisionless mechanism. For example, secondary electrons gain energy through a collisionless mechanism as they move from the negative potential imposed to the target to a higher potential in the plasma. Collisionless heating is facilitated by electric fields. In plasma with ionization zones, significant potential gradients exist in the axial, radial, as well as azimuthal directions (Figs. 5–7). As a consequence of the azimuthal potential gradients at the double layer, drifting electrons gain additional energy comparable to the energy gains from the axial potential gradient in the presheath. The energy gains can be understood considering the motion of electrons in **E**- and **B**-fields, which is determined by the equation

$$m_e \frac{d\mathbf{v}}{dt} = -e(\mathbf{E} + \mathbf{v} \times \mathbf{B}), \tag{7}$$

where $\mathbf{v}$ is velocity vector, $-e$ is the electron charge, and m_e is mass of an electron, respectively. If a scalar product of $\mathbf{v}$ is made with Eq. (7), we obtain the time derivative of electron's kinetic energy[52]

$$\frac{d}{dt}\left(\frac{m_e v^2}{2}\right) = e\mathbf{v} \cdot \mathbf{E}. \tag{8}$$

The second term on the right hand side of Eq. (7) vanishes when multiplying by $\mathbf{v}$ because $(\mathbf{v} \times \mathbf{B}) \cdot \mathbf{v} = 0$. According to Eq. (8), the change in the kinetic energy is solely determined by the electric field. The magnetic field does not change the kinetic energy of an electron because it exerts a force perpendicular to the velocity of an electron, changing its direction but not its magnitude.

Keeping in mind Eq. (8), the electrons obtain energy when they encounter an electric field (i.e., a potential gradient), such as the field in the double layer. The potential in the double layer jumps by 30–70 V in the region up to 20 mm over the racetrack area (see Figs. 5 and 6). Consequently, all drifting electrons, including those which were at first not capable of causing ionization, gain sufficient energy to ionize and excite gas when passing the potential jump of the double layer. After electrons cross the double layer, they start to lose their energy by inelastic collisions and therefore less excitation and ionization events occur as they drift away from the potential jump. The light from the ionization zone therefore becomes dimmer with increasing distance from the leading edge of the ionization zone (Fig. 4).

The long-held view in magnetron sputtering was that electron heating is mainly governed by hot secondary electrons (paradigm proposed by Thornton[53]). However, recent simulations of magnetron discharges suggest that Ohmic electron heating in the presheath is the dominant mechanism for sustaining the discharge.[54,55] These simulations were conducted for the traditional view of an azimuthally uniform discharge. More recently, this global ionization region model was reevaluated in light of azimuthally non-uniform plasma, and it was suggested that an underlying physical mechanism for the electron heating is related to the potential structure of the ionization zone.[46] More specifically, it was suggested that electrons gain energy when crossing from the low-potential side of the ionization zone to the high-potential side. These concepts have been so far supported by particle energy measurements[56] and by spectroscopically resolved snapshot-images of ionization zones.[57]

Electron energization ("heating") is important since the energetic electrons produce ion-electron pairs and are therefore critical to sustaining the discharge. In general, electron Ohmic heating refers to a power density, which, in its general form, is the product of the electron current density and electric field, $\mathbf{j}_e\mathbf{E}$. The heating power is associated with an acceleration of electrons in the electric field, and is not necessarily tied to collisions. In that sense, the here-described electron energization in a double layer is Ohmic heating. Following the prior work,[46] Ohmic heating appears to be highly localized involving electrons going to a higher potential, where the potential difference exceeds the ionization energy. Ohmic heating as viewed in this work thus includes two mechanisms: a collisionless mechanism where electrons gain energy from the potential jump (i.e., electric field of the double layer), and a collisional heating mechanism in which electrons gain energy via collisions when moving from lower to higher equipotential lines. The latter mechanism is not bound to an ionization zone and can occur anywhere, and involves the electron cross-**B**-field transport in radial and axial directions.

C. Spatial distribution and transport of ions, and implications for the motion of the ionization zone

Spatial distribution and transport of ions are essential for the magnetron sputtering process. Ions accelerated to the target determine the distribution of sputtered material, the erosion profile of the target, as well as the production of secondary electrons. Ions that are transported away from the target and reach the substrate are influential in the growth process of thin films (see, e.g., studies in Refs. 58–60). From our measurements, we can infer the approximate spatial distribution of the ion density by assuming that the ion density is approximately proportional to the light intensity of the ionization zone since the cross-sections for ionization and excitation of Ar are similar. This proposition is supported by spectroscopic images of ionization zones in HiPIMS, which showed that the highest ion densities are within the ionization zone.[57,61] If the light intensity is approximately proportional to the ion density, then, based on the reasoning of Section IV E, the spatial distribution of the ion density is similar to the spatial distribution of $V_p - V_f$ as presented in Figs. 10 and 11 and in supplementary materials S6 and S7. This means that the greatest rate of ionization occurs in the

regions of hottest electrons. Hence, Figs. 10 and 11, which are related to the energy of electrons, also approximately represent the spatial ion density distributions.

The transport of ions in magnetron discharges has not yet been satisfactory explained.[62] The motion of ions is determined by Eq. (7) (but using the ion mass and appropriate positive charge), where the second term ($\mathbf{v} \times \mathbf{B}$) can be neglected due to very large gyration radii of ions, meaning that ions in the magnetron plasma follow the local electric field direction. In the traditional view of azimuthally uniform plasma, the electric field points toward the racetrack region of the target. However, it is clear that some ions must encounter electric fields that allow them to escape from the target region and to contribute to film growth. Our data can provide some insight into this conundrum by considering the measured **E**-field distributions (Figs. 5–7, S4, and S5) and spatial ion density distributions (Figs. 10, 11, S6, and S7). The ion density is highest after the leading edge of the ionization zone and decreases in the $\mathbf{E}_z \times \mathbf{B}$ direction (see Figs. 10 and 11). Close to the target (e.g., up to 10 mm from the target), the **E**-field predominantly points towards the target (Fig. 6) suggesting that the spatial distribution of the sputtering rate and the secondary electron emission are similar to the spatial ion density distribution close to the target.

Remarkably, the direction of the **E**-field changes in the region further away from the target. Close inspection shows that the **E**-field in the high density plasma region (e.g., $\xi = 30°$–$150°$, $r = 15$–30 mm $z = 5$–20 mm) points away from this area (see Figs. 5–7). The electric field points in the radial and the axial directions: radially sideways from the racetrack area, axially toward the target and, interestingly, also axially away from the target. Hence, the **E**-field in the region of high plasma density accelerates ions away from the magnetron. The escape of ions is further promoted if the ion originated from an atom that had a high velocity component away from the target, which is the case for sputtered atoms. In our case of a low-current DCMS discharge, the electric field pointing away from the magnetron is weak but one can expect stronger fields (and higher atom and ion energies) in the case of high-current discharges (either in DCMS or in HiPIMS mode). The direction of the **E**-field in the *r*-*z* plane (i.e., $\mathbf{E}_{rz}$) changes considerably along the azimuth (see Figs. 7, S4, and S5). In the high-density region of plasma, $\mathbf{E}_{rz}$ points away from this area, as mentioned above, but in the low-density region, it funnels towards the racetrack area. Hence, ions experience very different transport along the plasma ring, and it can be presumed that a considerable fraction of them is transported away from the magnetron.

Besides the axial and radial electric fields, there is a strong azimuthal component ($\mathbf{E}_\xi$) particularly at the leading edge of the ionization zone, which points in the $-\mathbf{E}_z \times \mathbf{B}$ direction. This field does not only play an important role for the energization of electrons, as discussed earlier, but affects the motion and energy of ions as well. As one can see from Fig. 6, the **E**-field accelerates ions near the edge of the ionization zone in curved trajectories toward the target. This affects the displacement (motion) of the ionization zone in the $-\mathbf{E}_z \times \mathbf{B}$ direction, especially when also taking into account that those ions move in the $-\mathbf{E}_z \times \mathbf{B}$ direction and arrive at the target on the low plasma density side of the ionization zone. In the process, they generate secondary electrons, which in turn contribute to the ionization. The double layer, and therefore the entire ionization zone, moves in the same direction as the motion of ions near the zone's edge (i.e., in the $-\mathbf{E}_z \times \mathbf{B}$ direction). Hence, it can be argued that, in the case of low current DCMS discharges, the dynamics of ionization zone(s) is governed by the motion of ions at the leading edge of the ionization zone and formation of secondary electrons on the low plasma density side of the zone.

The $\mathbf{E}_\xi$-field also causes asymmetrical acceleration of ions in the $\mathbf{E}_z \times \mathbf{B}$ and $-\mathbf{E}_z \times \mathbf{B}$ directions. Indeed, such asymmetry was observed in our earlier experiments.[56] The asymmetry was thought to be associated with a moving potential hump.[39] Data presented here (e.g., Fig. 6) show a strong asymmetry in the potential structure and therefore suggests that the electric field direction of the double layer at the edge of the ionization zone plays a more important role than the zone's motion. Namely, ions accelerated by the strong $\mathbf{E}_\xi$-field at the edge of the ionization zone are subsequently accelerated to the target by the strong $\mathbf{E}_z$ component, while ions in the potential hump can escape and arrive at a substrate or ion detector. Such an observation was in fact made in Ref. 56 where we measured the *same* ion flux asymmetry for DCMS and HiPIMS discharges despite different directions of ionization zone motion for the two discharge modes.

D. Formation of a negative space charge before the double layer, and stability of the ionization zone

When magnetized electrons drift from a region of high plasma density into a region of lower plasma density, a net charge imbalance between ions and electrons must develop. In general, this imbalance can be attributed to the very different masses of electrons and ions, and thus to the different motions of electrons and ions above the magnetron's target. Figs. 8 and 9 show that the net charge in the azimuthal drift direction becomes increasingly negative as electrons drift away from the region of strong ionization. As a consequence of the Poisson equation, the plasma potential in this region becomes more negative, in a nonlinear way, as demonstrated in Figs. 5 and 6.

This effect is amplified by an argument made in Section IV C related to the motion of ions. Ions are accelerated to the target on the $-\mathbf{E}_z \times \mathbf{B}$ side of the potential jump due to the strong local **E**-field that is present there. The ion density on the low plasma density side is low not only because electrons have lost a large part of their energy before arriving at the double layer but also because ions are removed from this region by acceleration to the target. The combined effect creates a net negative space charge, which is represented by the dark blue region in Figs. 8 and 9.

For a given geometry, magnetic field, pressure, and discharge current, ionization zones are stable as they travel along the racetrack. We therefore find a sustained feedback relation between the potential structure, electron heating, and excitation and ionization processes as electrons drift in the magnetic trap of the magnetron. Namely, on one hand, electron energization enables the excitation and ionization, and

the formation of a net space charge double layer (positive after the potential jump, i.e., in the region of most ionization, and most negative before the jump), and on the other hand, the double layer governs the energization of electrons. The electron energization and the existence of the double layer are mutually self-sustaining; the potential jump re-supplies the energy to the electrons, and thereby electrons sustain the double layer.

E. Comparison of potential measurements with simulations from the literature

The measurements presented in this work are qualitatively in agreement with several findings in the recent literature. Most closely related to our experimental results is modeling of low current DCMS discharges performed by Pflug *et al.*[63] and Siemers *et al.*[64] They showed the formation of traveling ionization zones by using Particle-in-Cell (PIC) simulations and obtained a similar plasma potential distribution as measured in our experiments (cf. Fig. 6 from this study with Figure 7 from Ref. 63). Brenning *et al.*[45] investigated the effect of spokes and their potential distribution on the particle transport for HiPIMS discharges. They suggested that local space charges should be responsible for the spoke properties. In our experiments for DCMS, we indeed found the proposed space charge change from positive at the leading edge of the ionization zone to more negative values as electrons drift away from the edge. We additionally show a potential jump at the head of the zone, which makes the system consistent with the requirement that the plasma potential needs to return to the same value when the path over the racetrack is closed (at same radius r and height z): $\int (V_p(\xi) - \langle V_p \rangle)_{r,z}\, d\xi = 0$, where $\langle V_p \rangle$ designates the plasma potential averaged of the racetrack. In PIC-MCC (Particle-In-Cell Monte Carlo Collisions) simulations, Boeuf[65] investigated several $\mathbf{E} \times \mathbf{B}$ discharge geometries and found that for low pressure discharges, like those investigated here, significant deviations from quasi-neutral conditions can occur suggesting that electron and ion space charge regions are not specific but an essential feature of $\mathbf{E} \times \mathbf{B}$ discharges.

F. Implication of findings for ionization zones in HiPIMS

The findings presented here should also have implications for interpreting ionization zones in HiPIMS even as there are several features that distinguish the ionization zones in DCMS from the zones in HiPIMS discharges (see Section I). The most notable difference is the direction of zone motion; ionization zones in DCMS move in the $-\mathbf{E}_z \times \mathbf{B}$ direction while in HiPIMS, they move in the same direction as drifting electrons, $\mathbf{E}_z \times \mathbf{B}$ direction. The difference in the motion can be explained in terms of gas density distribution near the target and the motion/energization of electrons and ions through the double layer. In low current DCMS discharges, a relatively uniform gas distribution can be assumed above and along the racetrack. In such case, the displacement of zone(s) is governed by the motion and energization of electrons and ions near the potential jump as described in Section IV C. However, in HiPIMS discharges, the gas density near the target is strongly rarefied[66] and (self-) sputtering and gas-recycling[67] are predominantly localized to the ionization zones. This suggests that the gas density is modulated along the racetrack. One could therefore speculate that, in the case of HiPIMS, electrons need to travel further into the ionization zone in order to encounter the to-be-ionized neutrals and, as a consequence, the ionization zones should move in the same direction as drifting electrons, which are observed for HiPIMS discharges.[4,8,11]

Furthermore, other features of ionization zones in HiPIMS discharges can be interpreted using the above reasoning. For similar gas pressures, the ionization zones in HiPIMS are azimuthally shorter, more numerous, and not as stable compared to ionization zones in DCMS. These characteristics can be attributed to a combination of electron energies and gas density. As already suggested in Ref. 6, electrons predominantly interact with the background gas in DCMS, while in HiPIMS discharges, electrons interact with atoms from the target (sputtered and outgassed). The latter can be modulated in HiPIMS because the ionization occurs very close to the target (millimeters) and the refill time is determined by the sputtered atoms, which travel from the target to the location of the ionization. More importantly, the sputtering rate (not the deposition rate) during the HiPIMS pulse is higher due to several magnitudes larger discharge current than in DCMS. One can also expect a slightly higher sputtering yield in HiPIMS due to higher applied voltages to the cathode. Both of these facts should result in azimuthally non-uniform supply of sputtered (and outgassed) atoms with large gas density within the ionization zones than between the ionization zones. Hence, we anticipate that the gas density near the target surface is modulated in the azimuthal direction and closely coincides with the light intensity. The modulation occurs due to the supply of sputtered (and outgassed) atoms from the ionization zones and not primarily due to refilling of the gas from the surrounding atmosphere. Besides, the ionization cross-section for the sputtered metal atoms is higher than for noble gases. The dynamics of ionization zones in HiPIMS should therefore depend on the target material which is indeed documented in the literature (see, e.g., Refs. 4 and 8). All of above reasons can explain shorter, more numerous, and more dynamically changing ionization zones in HiPIMS than in DCMS. Clearly, properties and dynamics of ionization zones in HiPIMS are more complicated due to the combined effects of self-sputtering, gas rarefaction, gas recycling, near-target gas modulation, and other self-amplifying mechanisms, which result in the overall non-stationary conditions of the discharge.

V. SUMMARY AND CONCLUSIONS

For low-current DC magnetron discharges, space- and time-resolved floating and plasma potential distributions have been measured using a cold and a hot emissive probe. From the potential data, we could derive the local electric field and the net space charge distributions which travel with the ionization zone along the target's racetrack. Data are visualized from several projection planes together with animations and additional figures, which can be found in the

supplementary material. From these data, we could build a more detailed picture of ionization zone properties. The leading edge of the ionization zone is characterized by an electric double layer, energizing drifting electrons, which can further cause ionization and excitation. Before crossing the double layer, electrons are at the lowest potential, while in the potential hump, after the double layer, they are at the highest potential. This supports the suggestion that not only secondary electrons but also electrons created in the plasma are capable of gas ionization once they cross and obtain energy from the potential jump. The hump is very asymmetric, showing a steep rise at the front end and then a gradual slope toward the trailing end. Electrons drifting in the $\mathbf{E}_z \times \mathbf{B}$ direction from the denser plasma of the ionization zone into a region of lower plasma density cause a slight imbalance of charge, with an increasingly negative net charge forming before the double layer. A large charge imbalance around the leading edge of the ionization zone is sustained by a strong azimuthal electric field that accelerates ions in the $-\mathbf{E}_z \times \mathbf{B}$ direction and towards the target. The space charge and related field structure can explain many features observed, including the ionization zone motion and azimuthally asymmetric ion emissions. We show that the zone's shape, ionization, and light emission intensity are related to the potential structure and local distribution of the energy of electrons. While the measurements and interpretation are related to DCMS, many of the features may also be associated with the ionization zones in HiPIMS.

SUPPLEMENTARY MATERIAL

See supplementary material for

S1: Reproducibility of the plasma potential (V_p) and the floating potential (V_f) recorded at $r = 24$ mm and different axial distances from the surface of the target. Five signals recorded in the separation of few seconds are shown for each axial position.

S2: Target potential as a function of probes' (a) radial and (b) axial positions.

S3: Potential on the emissive probe as a function of filament heating current. Measurements were recorded at $z = 15$ mm and $r = 24$ mm.

S4: Plasma potential and electric field distributions in the r-z plane of the magnetron for different azimuthal angles.

S5: Animation of plasma potential and electric field distribution in the r-z plane of the magnetron for azimuthal angles in 5° steps.

S6: Distribution of $V_p - V_f$ in the r-z plane for different azimuthal angles.

S7: Animation of $V_p - V_f$ distributions in the r-z plane for azimuthal angles in 5° steps.

ACKNOWLEDGMENTS

M. Panjan gratefully acknowledges the financial support of project No. J2-7238 and USA-Slovenian bilateral project No. BI-US/16-17-052 funded by the Slovenian Research Agency. Work at Lawrence Berkeley National Laboratory is supported by the U.S. Department of Energy under Contract No. DE-AC02-05CH11231.

[1]W. D. Gill and E. Kay, Rev. Sci. Instrum. **36**, 277 (1965).
[2]D. Depla and S. Mahieu, *Reactive Sputter Deposition* (Springer, Berlin, 2008).
[3]A. Kozyrev, N. Sochugov, K. Oskomov, A. Zakharov, and A. Odivanova, Plasma Phys. Rep. **37**, 621 (2011).
[4]A. Anders, P. Ni, and A. Rauch, J. Appl. Phys. **111**, 053304 (2012).
[5]A. P. Ehiasarian, A. Hecimovic, T. de los Arcos, R. New, V. Schulz-von der Gathen, M. Boke, and J. Winter, Appl. Phys. Lett. **100**, 114101 (2012).
[6]M. Panjan, S. Loquai, J. E. Klemberg-Sapieha, and L. Martinu, Plasma Sources Sci. Technol. **24**, 065010 (2015).
[7]A. Anders, P. Ni, and J. Andersson, IEEE Trans. Plasma Sci. **42**, 2578 (2014).
[8]A. Hecimovic, C. Maszl, V. Schulz-von der Gathen, M. Böke, and A. von Keudell, Plasma Sources Sci. Technol. **25**, 035001 (2016).
[9]Y. Yang, X. Zhou, J. X. Liu, and A. Anders, Appl. Phys. Lett. **108**, 034101 (2016).
[10]A. Hecimovic, V. Schulz-von der Gathen, M. Böke, A. von Keudell, and J. Winter, Plasma Sources Sci. Technol. **24**, 045005 (2015).
[11]Y. Yang, J. Liu, L. Liu, and A. Anders, Appl. Phys. Lett. **105**, 254101 (2014).
[12]S. M. Rossnagel and H. R. Kaufman, J. Vac. Sci. Technol. A **4**, 1822 (1986).
[13]T. E. Sheridan, M. J. Goeckner, and J. Goree, J. Vac. Sci. Technol. A **9**, 688 (1991).
[14]M. Spolaore, V. Antoni, M. Bagatin, A. Buffa, R. Cavazzana, D. Desideri, E. Martines, N. Pomaro, G. Serianni, and L. Tramontin, Surf. Coat. Technol. **116–119**, 1083 (1999).
[15]D. Field, S. Dew, and R. Burrell, J. Vac. Sci. Technol. A **20**, 2032 (2002).
[16]P. Špatenka, J. Vlček, and J. Blažek, Vacuum **55**, 165 (1999).
[17]J. Bradley, S. Thompson, and Y. A. Gonzalvo, Plasma Sources Sci. Technol. **10**, 490 (2001).
[18]S. Z. Wu, J. Appl. Phys. **98**, 083301 (2005).
[19]A. Solov'ev, N. Sochugov, K. Oskomov, and S. Rabotkin, Plasma Phys. Rep. **35**, 399 (2009).
[20]S.-H. Seo and H.-Y. Chang, Phys. Plasmas **11**, 3595 (2004).
[21]S.-H. Seo, J.-H. In, and H.-Y. Chang, J. Appl. Phys. **97**, 023305 (2005).
[22]B. B. Sahu, J. G. Han, H. R. Kim, K. Ishikawa, and M. Hori, J. Appl. Phys. **117**, 033301 (2015).
[23]P. Sigurjonsson and J. T. Gudmundsson, J. Phys.: Conf. Ser. **100**, 062018 (2008).
[24]P. Poolcharuansin, B. Liebig, and J. Bradley, IEEE Trans. Plasma Sci. **38**, 3007 (2010).
[25]P. Sigurjonsson, Ph.D. thesis, Reykjavik Faculty of Engineering, University of Iceland, 2008.
[26]A. Mishra, P. J. Kelly, and J. W. Bradley, J. Phys. D: Appl. Phys. **44**, 425201 (2011).
[27]A. Rauch, R. J. Mendelsberg, J. M. Sanders, and A. Anders, J. Appl. Phys. **111**, 083302 (2012).
[28]J. W. Bradley, H. Bäcker, P. J. Kelly, and R. D. Arnell, Surf. Coat. Technol. **135**, 221 (2001).
[29]J. W. Bradley, H. Bäcker, P. J. Kelly, and R. D. Arnell, Surf. Coat. Technol. **142–144**, 337 (2001).
[30]A. Vetushka, S. K. Karkari, and J. W. Bradley, J. Vac. Sci. Technol. A **22**, 2459 (2004).
[31]A. Palmero, E. D. van Hattum, W. M. Arnoldbik, A. M. Vredenberg, and F. H. P. M. Habraken, J. Appl. Phys. **95**, 7611 (2004).
[32]A. Palmero, E. D. van Hattum, H. Rudolph, and F. H. P. M. Habraken, Thin Solid Films **494**, 18 (2006).
[33]E. Martines, R. Cavazzana, G. Serianni, M. Spolaore, L. Tramontin, M. Zuin, and V. Antoni, Phys. Plasmas **8**, 3042 (2001).
[34]E. Martines, M. Zuin, V. Antoni, R. Cavazzana, G. Serianni, M. Spolaore, and C. Nakashima, Phys. Plasmas **11**, 1938 (2004).
[35]E. Martines, M. Zuin, R. Cavazzana, J. Adámek, V. Antoni, G. Serianni, M. Spolaore, and N. Vianello, Phys. Plasmas **21**, 102309 (2014).
[36]A. Hecimovic, M. Böke, and J. Winter, J. Phys. D: Appl. Phys. **47**, 102003 (2014).
[37]L. Meng, H. Yu, M. M. Szott, J. T. McLain, and D. N. Ruzic, J. Appl. Phys. **115**, 223301 (2014).
[38]N. Hershkowitz, *Plasma Diagnostics: Discharge Parameters and Chemistry* (Elsevier Science, 1989).
[39]A. Anders, M. Panjan, R. Franz, J. Andersson, and P. Ni, Appl. Phys. Lett. **103**, 144103 (2013).
[40]P. Balan, R. Schrittwieser, C. Ioniţă, J. A. Cabral, H. F. C. Figueiredo, H. Fernandes, C. Varandas, J. Adámek, M. Hron, J. Stöckel, E. Martines, M. Tichý, and G. Van Oost, Rev. Sci. Instrum. **74**, 1583 (2003).
[41]R. Schrittwieser, C. Ionita, P. C. Balan, J. A. Cabral, F. H. Figueiredo, V. Pohoata, and C. Varandas, Contrib. Plasma Phys. **41**, 494 (2001).

[42]T. E. Sheridan, M. J. Goeckner, and J. Goree, J. Vac. Sci. Technol. A **16**, 2173 (1998).
[43]A. Anders, Surf. Coat. Technol. **205**, S1 (2011).
[44]J. M. Sanders, A. Rauch, R. J. Mendelsberg, and A. Anders, Rev. Sci. Instrum. **82**, 093505 (2011).
[45]N. Brenning, D. Lundin, T. Minea, C. Costin, and C. Vitelaru, J. Phys. D: Appl. Phys. **46**, 084005 (2013).
[46]A. Anders, Appl. Phys. Lett. **105**, 244104 (2014).
[47]A. Anders, Appl. Phys. Lett. **100**, 224104 (2012).
[48]N. Britun, M. Palmucci, S. Konstantinidis, and R. Snyders, J. Appl. Phys. **117**, 163302 (2015).
[49]N. Britun, M. Palmucci, S. Konstantinidis, and R. Snyders, J. Appl. Phys. **117**, 163303 (2015).
[50]C. Charles, Plasma Sources Sci. Technol. **16**, R1 (2007).
[51]L. P. Block, Astrophys. Space Sci. **55**, 59 (1978).
[52]M. A. Lieberman and A. J. Lichtenberg, *Principles of plasma discharges and materials processing* (Wiley-Interscience, Hoboken, New Jersey, 2005).
[53]J. A. Thornton, J. Vac. Sci. Technol. **15**, 171 (1978).
[54]C. Huo, D. Lundin, M. A. Raadu, A. Anders, J. T. Gudmundsson, and N. Brenning, Plasma Sources Sci. Technol. **22**, 045005 (2013).
[55]N. Brenning, J. Gudmundsson, D. Lundin, T. Minea, M. Raadu, and U. Helmersson, Plasma Sources Sci. Technol. **25**, 065024 (2016).
[56]M. Panjan, R. Franz, and A. Anders, Plasma Sources Sci. Technol. **23**, 025007 (2014).
[57]J. Andersson, P. Ni, and A. Anders, Appl. Phys. Lett. **103**, 054104 (2013).
[58]T. Jäger, Y. E. Romanyuk, A. N. Tiwari, and A. Anders, J. Appl. Phys. **116**, 033301 (2014).
[59]R. Franz, C. Clavero, J. Kolbeck, and A. Anders, Plasma Sources Sci. Technol. **25**, 015022 (2016).
[60]V. Stranak, Z. Hubicka, M. Cada, S. Drache, M. Tichy, and R. Hippler, J. Appl. Phys. **115**, 153301 (2014).
[61]P. Poolcharuansin, F. L. Estrin, and J. W. Bradley, J. Appl. Phys. **117**, 163304 (2015).
[62]J. T. Gudmundsson, N. Brenning, D. Lundin, and U. Helmersson, J. Vac. Sci. Technol. A **30**, 030801 (2012).
[63]A. Pflug, M. Siemers, T. Melzig, L. Schäfer, and G. Bräuer, Surf. Coat. Technol. **260**, 411 (2014).
[64]M. Siemers, A. Pflug, T. Melzig, K. Gehrke, A. Weimar, and B. Szyszka, Surf. Coat. Technol. **241**, 50 (2014).
[65]J.-P. Boeuf, Front. Phys. **2**, 74 (2014).
[66]M. Palmucci, N. Britun, S. Konstantinidis, and R. Snyders, J. Appl. Phys. **114**, 113302 (2013).
[67]A. Anders, J. Čapek, M. Hála, and L. Martinu, J. Phys. D: Appl. Phys. **45**, 012003 (2012).